Oxygen-Deficient β-MnO$_2$@Graphene Oxide Cathode for High-Rate and Long-Life Aqueous Zinc Ion Batteries

Shouxiang Ding[1], Mingzheng Zhang[1], Runzhi Qin[1], Jianjun Fang[1], Hengyu Ren[1], Haocong Yi[1], Lele Liu[1], Wenguang Zhao[1], Yang Li[1], Lu Yao[1], Shunning Li[1] ✉, Qinghe Zhao[1] ✉, Feng Pan[1] ✉

HIGHLIGHTS

- The concurrent application of vacancy enrichment and surface coating in β-MnO$_2$ electrode can both improve the intercalation kinetics and inhibit the Mn dissolution.

- The oxygen-deficient β-MnO$_2$@graphene oxide electrode delivers a reversible capacity of 129.6 mAh g^{-1} after 2000 cycles at 4C, outperforming the state-of-the-art MnO$_2$-based cathodes.

- The excellent performance is rooted in the strong binding of graphene oxide on defective β-MnO$_2$ and the regulated structural evolution into the Zn$_x$Mn$_2$O$_4$ phase.

ABSTRACT Recent years have witnessed a booming interest in grid-scale electrochemical energy storage, where much attention has been paid to the aqueous zinc ion batteries (AZIBs). Among various cathode materials for AZIBs, manganese oxides have risen to prominence due to their high energy density and low cost. However, sluggish reaction kinetics and poor cycling stability dictate against their practical application. Herein, we demonstrate the combined use of defect engineering and interfacial optimization that can simultaneously promote rate capability and cycling stability of MnO$_2$ cathodes.

β-MnO$_2$ with abundant oxygen vacancies (V$_O$) and graphene oxide (GO) wrapping is synthesized, in which V$_O$ in the bulk accelerate the charge/discharge kinetics while GO on the surfaces inhibits the Mn dissolution. This electrode shows a sustained reversible capacity of ∼ 129.6 mAh g^{-1} even after 2000 cycles at a current rate of 4C, outperforming the state-of-the-art MnO$_2$-based cathodes. The superior performance can be rationalized by the direct interaction between surface V$_O$ and the GO coating layer, as well as the regulation of structural evolution of β-MnO$_2$ during cycling. The combinatorial design scheme in this work offers a practical pathway for obtaining high-rate and long-life cathodes for AZIBs.

KEYWORDS Manganese oxides; Oxygen defects; Surface optimization; Aqueous zinc battery
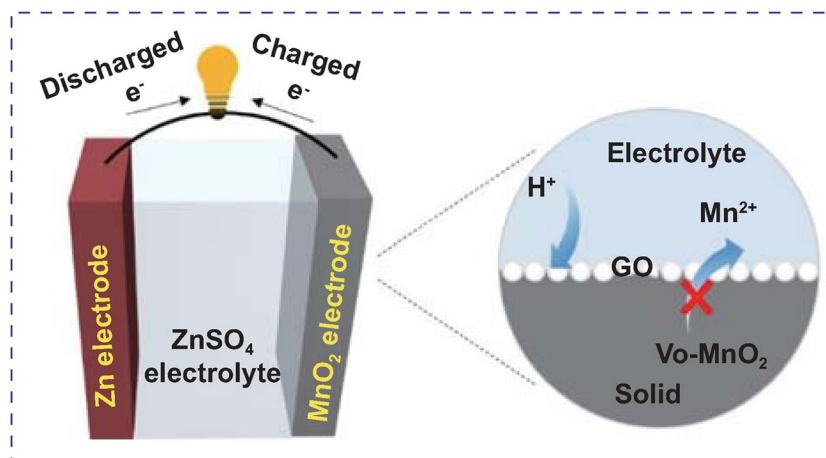
✉ Shunning Li, lisn@pku.edu.cn; Qinghe Zhao, zhaoqh@pku.edu.cn; Feng Pan, panfeng@pkusz.edu.cn
[1] School of Advanced Materials, Peking University Shenzhen Graduate School, Shenzhen 518055, People's Republic of China

1 Introduction

The worldwide transition from fossil fuels to sustainable energy sources has spawned a rising demand for more reliable and low-cost batteries in the field of large-scale energy storage [1], where safety and economic issues are more of a concern than energy density. Rechargeable aqueous zinc ion batteries (AZIBs) [2], because of their non-flammability, cost effectiveness, environmental benignity, and abundant sources, offer a promising alternative to the lithium-ion battery technology in stationary grid-connected applications. Currently, the performance of AZIBs is largely limited by available cathode materials, of which renowned examples include manganese oxides [3], vanadium oxides [4], Prussian blue analogs [5, 6], and organic species [7]. Among them, polymorphs of MnO_2 have captured particular attention due to their outstanding theoretical capacity and a preferable theoretical voltage versus Zn anode [8–12]. However, the development of MnO_2 cathodes has been impeded by scientific challenges related to the kinetic limitations and capacity fading, which can be ascribed to the sluggish Zn^{2+} diffusion in the cathode [13] and the irreversible phase transformation [14], respectively. To realize high-rate and long-life AZIBs, it is therefore required to formulate new design strategies for MnO_2-based cathode materials.

Toward this goal, researchers have adopted various technologies, including pre-intercalation engineering [15], defect engineering [16, 17], interfacial optimization [18, 19], and metal-doping [20], etc. Especially, the incorporation of oxygen vacancies (V_O) is an effective route to improve the rate performance of MnO_2 electrodes. Previous studies have suggested that electronic conductivity can be enhanced in the presence of V_O [21, 22] and that the under-coordinated Mn ions will potentially afford facile transport pathways for ionic charge carriers [23–26]. It is worth mentioning that a recent study of β-MnO_2 cathode has revealed the massive proton insertion triggered by the introduction of V_O into the bulk lattice [27]. These promising aspects enabled by oxygen deficiency may, however, be tarnished by a higher susceptibility to Mn dissolution, which is likely to incur phase transitions. In this regard, surface coating (SC) can be leveraged to inhibit the Mn ions diffusing into the electrolyte. For pristine MnO_2 cathodes, the benefits of SC have already been demonstrated in several reports with carbon-based coating materials ranging from graphene [28, 29] to polymers [30, 31].

Yet, the pertinent combination of V_O and SC has not been explored in AZIB cathodes up to date, despite its fascinating potential to promote rate capability and cycling stability at the same time. Moreover, how such coatings interact with MnO_2 is rarely discussed, thus depriving researchers of a rational understanding of the role played by SC.

In this work, we report the combinatorial use of defect engineering and interfacial optimization to boost the electrochemical performance of β-MnO_2 cathode. Electrode with excessive V_O and graphene oxide (GO) wrapping is directly synthesized via a simple hydrothermal reaction. V_O plays the vital role in facilitating the transfer of electrons and protons, while GO coating suppresses the dissolution of Mn ions. As a consequence, the oxygen-deficient β-MnO_2@graphene oxide architecture exhibits high capacity, superior charge/discharge rates, and excellent cycle stability. Our work highlights that the tight binding of GO to the surfaces of β-MnO_2 via the interaction with V_O acts in synergy with the regulated formation of spinel $Zn_xMn_2O_4$ to guarantee the structural integrity of the electrode during long-term cycling.

2 Experimental Section

2.1 Synthesis of β-MnO_2@GO Nanorods

The β-MnO_2@GO nanorod was synthesized via a typical hydrothermal method. 30 mL 0.6 M $MnSO_4$, 2 mL 0.5 M H_2SO_4, and 4 mL 1 mg mL^{-1} GO dispersed aqueous solutions were mixed and continuously stirred for 30 min. 30 mL 0.1 M $KMnO_4$ was then added into the resultant solution dropwise, after which the solution was stirred at room temperature for another 30 min and then loaded into a 100 mL Teflon-lined autoclave and maintained at 120 °C for 12 h. Finally, the obtained products were collected by the filter and were washed with deionized water and absolute ethyl alcohol for three times, respectively, and then dried at 80 ℃ for 12 h. The β-MnO_2 counterpart was synthesized with the same method without adding GO.

2.2 Materials Characterization

The prepared materials were characterized by X-ray diffraction (XRD, Bruker D8 ADVANCE) with Cu Kα radiation. Scanning electron microscopy (SEM, ZEISS SUPRA55) and

transmission electron microscopy (TEM, JEM-3200FS) were employed to investigate the micromorphology and micro-structure. The thermogravimetric analysis (TGA) data were recorded in O_2 atmosphere using a 10 ℃ min^{-1} heating rate from 30 to 700 ℃. X-ray photoelectron spectroscopy (XPS, ESCALAB 250Xi) was used to conduct the element composition and electronic structure analysis, in company with the energy-dispersive spectroscopy (EDS, Oxford X-Max 20) and Fourier transform infrared spectroscopy (FTIR). Electron paramagnetic resonance (EPR, Bruker A300-10/12) was performed to characterize the unpaired electron.

2.3 Electrochemical Tests

Electrochemical performance was tested in CR2032-type coin cells which were assembled in air condition. The working cathodes were fabricated by blending active materials, acetylene black (AB) and polyvinylidene fluoride (PVDF) in a weight ratio of 7:2:1 with N-methyl-2-pyrrolidone (NMP) used as a solvent to form a viscous slurry and coat onto Ti foil. The areal active loading for both the β-MnO_2 and β-MnO_2@GO is about ~ 2 mg cm^{-2}. The as-prepared electrodes were dried in vacuum oven of about 110 ℃ for 24 h. Zinc foil in 10 mm and glass fiber membrane in 16 mm were used as the anode and separator, respectively. The electrolyte contained 3 M $ZnSO_4$ and 0.2 M $MnSO_4$ in aqueous solution. The LAND-CT2001A battery-testing instrument was conducted for cycle and rate test with assembled cells. EIS was performed on a Chi 660e electrochemical workstation with frequency range from 100 kHz to 0.1 Hz.

2.4 First Principles Calculations

Density functional theory (DFT) calculations were carried out using projected augmented wave pseudopotentials and the generalized gradient approximation in the form of the Perdew–Burke–Ernzerhof exchange–correlation functional modified for solids (PBEsol), as embedded in Vienna ab initio simulation package (VASP). The van der Waals interactions were treated using Grimme's correction (DFT-D3). To deal with the localization of d electrons on Mn ions, Hubbard-corrected PBEsol+U(+J) functional was employed. More details are given in the Supporting Information.

3 Results and Discussion

3.1 Material Characterization

XRD patterns of the prepared β-MnO_2 and β-MnO_2@GO are shown in Fig. 1a, which match very well with the standard β-MnO_2 (tetragonal, space group of P42/mnm, PDF #42-0735). This result indicates that GO wrapping does not alter the crystal structure of the β-MnO_2. SEM results show the nanorod morphologies of β-MnO_2 and β-MnO_2@GO with several micrometers in length and 200–300 nm in width (Fig. S1). The high-resolution TEM (HRTEM) confirms the adhesion of GO to the surfaces of β-MnO_2 (Fig. 1b). Two lattice fringes of (101) and (110) planes are observed for β-MnO_2@GO (Fig. 1c), with interlayer spacing values of ~ 2.40 and ~ 3.13 Å, respectively, consistent with the XRD results in Fig. 1a. Similar lattice fringe results are also observed for β-MnO_2 (Fig. S2). There exist some ambiguous areas in β-MnO_2@GO, which can be ascribed to the formation of a large number of defects.

EDS, FTIR, and XPS further justify the successful wrapping of GO (Fig. 1b) in the β-MnO_2@GO sample. Figure 1d reveals the uniform distributions of Mn, O, and trace amount of C elements. Comparison of FTIR results in Fig. 1e demonstrates the characteristic peaks of C-O (~ 1432 cm^{-1}) and C=C (~ 1576 cm^{-1}) [32] in β-MnO_2@GO. Three clear peaks located at ~ 284.8, ~ 286.0, and ~ 288.8 eV in XPS C 1 s spectrum of β-MnO_2@GO (Fig. 1f) indicate the existence of C–C/C=C, C–O, and O–C=O bonds, respectively.

The formation of V_O can be implied by the XPS O 1s spectra (Fig. 1g), where the characteristic peak of V_O (~ 531.2 eV) in β-MnO_2@GO is substantially higher than that in β-MnO_2. EPR spectra (Fig. S3) showing an apparent symmetrical signal at $g = 2.0$ also suggest the high concentration of V_O [33]. The TGA curves of β-MnO_2 and β-MnO_2@GO in O_2-containing atmosphere are shown in Fig. 1h. In the temperature range of 200–600 °C, the TGA curve of β-MnO_2@GO rises, indicating the filling of V_O by oxygen, in contrast to the β-MnO_2 sample where the mass change is negligible. Here, we cannot rule out the possibility of GO decomposition, which will contribute to mass loss. Due to the formation of more V_O, Mn ions in β-MnO_2@GO show lower valence than those in β-MnO_2,
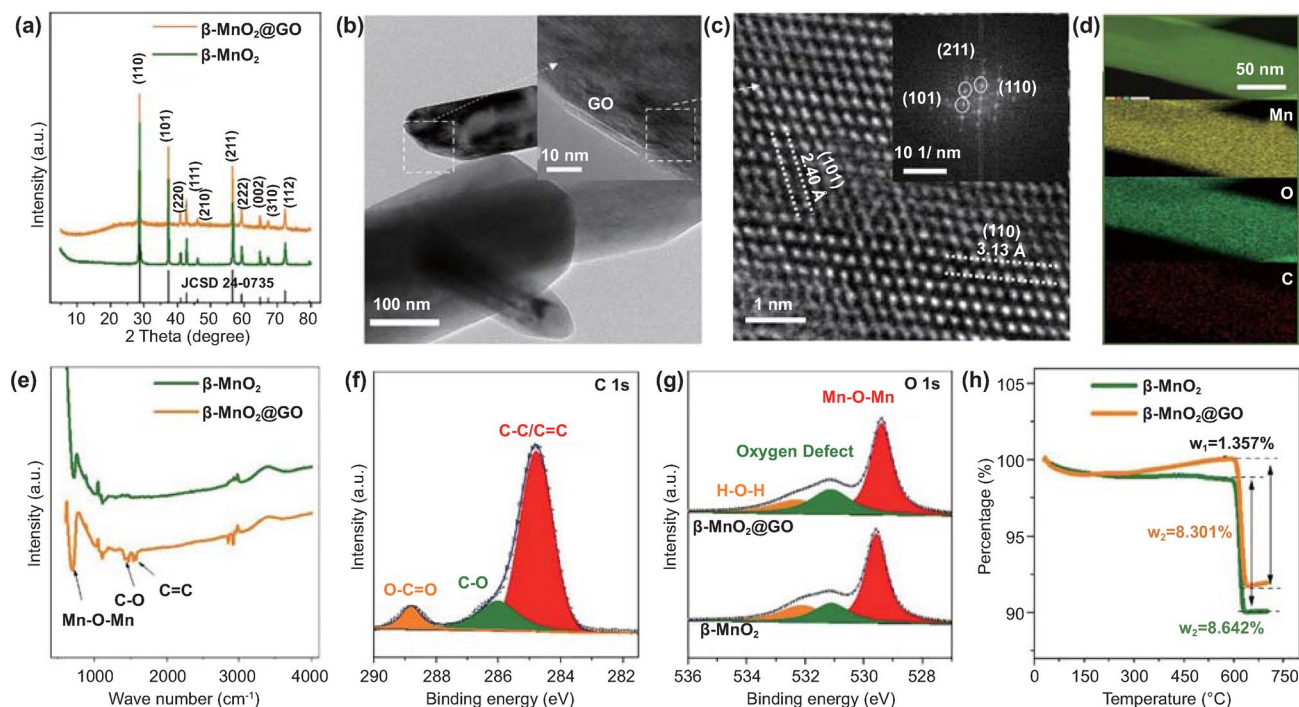
Fig. 1 **a** XRD patterns of β-MnO$_2$ and β-MnO$_2$@GO. **b–d** TEM, HRTEM morphologies, and correlated EDS mapping results of β-MnO$_2$@GO (the insets in **b** and **c** show the presence of GO layer and the diffraction pattern, respectively). **e** comparison of FTIR spectra of β-MnO$_2$ and β-MnO$_2$@GO. **f** XPS peaks of C 1s and **g** O 1s spectra. **h** TGA curves of β-MnO$_2$ and β-MnO$_2$@GO in an O$_2$-containing atmosphere

as revealed by Mn 3s spectra in Fig. S4. Such a remarkable increase in V$_O$ concentration is associated with both the low average oxidation state of Mn (+2.7) in the reactant solution, and the deoxygenation of GO during hydrothermal process, which will develop a strong tendency to extract the surface O ions of the as-produced β-MnO$_2$ so as to compensate the abundant dangling bonds on the reduced GO. The functional groups on GO may also accelerate the formation of β-MnO$_2$, in which case the fast kinetics will potentially give rise to offset from the equilibrium state, for example, in the form of bulk V$_O$. This scenario is similar to the cases of TiO$_2$@GO [34] and other MnO$_2$@GO electrodes in previous report, where the generation of V$_O$ in the transition metal oxides can be triggered during their hydrothermal growth in the presence of GO [35–37].

3.2 Electrochemical Performance

Coin-type cells are assembled with Zn plate as anode and aqueous 3 M ZnSO$_4$ + 0.2 M MnSO$_4$ as electrolyte. The role of the pre-added Mn^{2+} in the electrolyte is to suppress the

Mn^{2+} dissolution upon discharge processes, and the optimized Mn^{2+} concentration in electrolyte is ~0.2 M (Fig. S5). Figure 2a compares the rate performance of the β-MnO$_2$ and β-MnO$_2$@GO electrodes. It can be seen that both electrodes show similar capacity activation process in the initial eight cycles at a current of 0.1C (1C = 308 mA g^{-1}), indicating that GO wrapping shows little influence on the capacity delivery of β-MnO$_2$ at low current rates. After eight cycles, the discharge capacity of β-MnO$_2$@GO is stabilized at ~322.6 mAh g^{-1}. Figure 2b shows the galvanostatic charge/discharge (GCD) curves of the β-MnO$_2$ and β-MnO$_2$@GO electrodes at a current of 0.1C in the second cycle, indicating that GO wrapping can induce an elevated discharge platform, i.e., a smaller polarization. Figures 2c and S6 show the GCD curves of the β-MnO$_2$@GO and β-MnO$_2$ electrodes at various current rates, respectively. The discharge capacities of β-MnO$_2$@GO are ~312.4, ~290.9, ~259.6, ~211.7, ~158.6, ~132.5, ~106.8, and ~94.9 mAh g^{-1} at current rates of 0.25, 0.5, 1, 2, 4, 6, 8, and 10C, respectively, which are much higher than those of β-MnO$_2$.

Figure 2d, e provides the cycling performances of β-MnO$_2$ and β-MnO$_2$@GO electrodes at current rates of 1C and 4C,
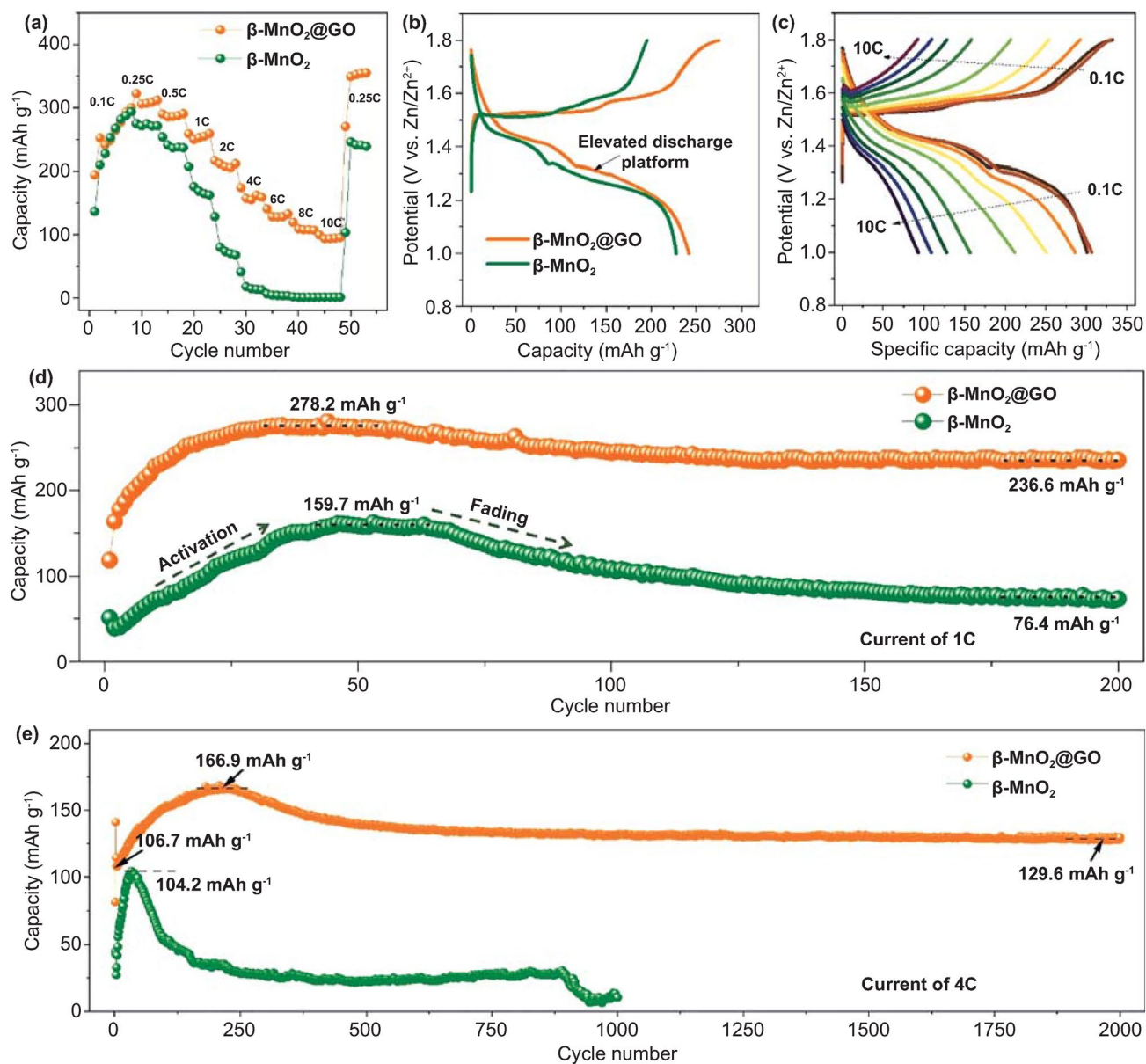
Fig. 2 **a**, **b** Comparison of rate performances and the galvanostatic charge/discharge (GCD) curves at the second cycle (at current of 0.1C) of β-MnO$_2$ and β-MnO$_2$@GO electrodes. **c** GCD curves of β-MnO$_2$@GO electrodes at various rate currents. Cycling performances of β-MnO$_2$ and β-MnO$_2$@GO electrodes at the rate currents of **e** 1C and **f** 4C

respectively. It can be seen that the cycling performances follow the similar trend: The discharge capacity is activated in the initial cycles and then continuously reduces in the subsequent cycles. This kind of capacity variation is similar to other manganese oxide electrodes in previous reports [38, 39], and the initial capacity activation process can be attributed to the bulk-nanocrystalline evolution during cycling. For β-MnO$_2$@GO, at a current rate of 1C, the discharge

capacity first increases to ~278.6 mAh g^{-1} in 50 cycles and then reduces slowly to ~236.6 mAh g^{-1} in 200 cycles. Furthermore, at a current rate of 4C, the discharge capacity first increases to ~166.9 mAh g^{-1} in 220 cycles and then reduces slowly to ~129.6 mAh g^{-1} in 2000 cycles, with nearly no capacity fading as compared with the initial discharge capacity (~106.7 mAh g^{-1}). The capacity, rate, and cycling performances of β-MnO$_2$@GO are among the best reported

manganese oxides (Table S1). Therefore, the combination of V_O and GO wrapping on β-MnO_2 not only enhances the charge/discharge kinetics for superior rate performances, but also improves the cycling stability of the electrode.

3.3 Charge Storage Mechanism

Insights into the charge storage mechanism is highly significant to understand the enhanced electrochemical performances of β-MnO_2@GO. Herein, XRD, SEM, TEM, and XPS are comprehensively applied to reveal the charge storage mechanism and the correlated structural evolution of β-MnO_2@GO upon cycles. Figure 3a shows the GCD curves of β-MnO_2@GO electrode in the initial two cycles (at current rate of 0.1C), with the correlated XRD patterns at selected states (from point #A to #J) given in Fig. 3b. It can be seen that the (110), (101), (211) peaks of β-MnO_2@GO located at 28.62°, 37.28°, 56.60° shift negligibly upon discharge/charge processes. After discharge (i.e., at point #B in the first cycle, and point #H in the second cycle), two diffraction peaks at 16.35° and 33.95° emerge, corresponding well to the monoclinic MnOOH (orthorhombic, Pnma (62), PDF #88-0648), a typical product of proton conversion in MnO_2 [40, 41]. Meanwhile, zinc sulfate hydroxide hydrate by-product ($Zn_4(OH)_6·ZnSO_4·xH_2O$, abbreviated as "ZSH," PDF #44-0673) is generated upon discharge, featuring a set of strong diffraction peaks located at 8.12°, 15.08°, 21.56°, and 24.57°, which is a critical evidence for proton intercalation into the lattice framework of MnO_2 [20]. The presence of ZSH on the electrode can be further confirmed by the morphology evolutions of β-MnO_2@GO electrodes, (Figs. 3c, S7), and the detailed analysis for the morphology evolutions is shown in Supporting Information.

As reported previously, for β-MnO_2, protons rather than Zn^{2+} ions tend to intercalate into the [1 × 1] tunnel framework, owing to the large ion radius and high charge density of the divalent Zn^{2+} ions [24]. Hence, the charge storage in β-MnO_2@GO is likely to be dominated by the proton intercalation/conversion reactions. When the amount of intercalated proton in surface area exceeds a threshold, it converts to the orthorhombic MnOOH, which explains the co-existence of diffraction patterns of MnOOH (surface area) and protonated β-H_xMnO_2 (internal area) phases [27] upon discharge in Fig. 3b. Furthermore, some weak peaks locating at 32.97° and 58.70° are observed upon discharge

in the second cycle, which is indexed to the $ZnMn_2O_4$ phase (hetaerolite, 141/amd, PDF No. 24-1133) [3, 42]. HRTEM is also applied to reveal the lattice structures of β-H_xMnO_2, MnOOH, and $ZnMn_2O_4$ phases in the discharged electrode, as shown in Fig. 3d–g. The nanorod morphology of β-MnO_2@GO maintains well upon discharge. We note that the internal part (region I) remains the pristine crystal lattice of β-MnO_2 (Fig. 3e), while the surface parts (i.e., in region II and III) show a different scenario. The magnified HRTEM images and the correlated diffraction patterns in region II and III (Fig. 3f, g) show the lattice fringes corresponding to (200) plane of MnOOH and (103) plane of $ZnMn_2O_4$, respectively. The detailed analyses of diffraction patterns from regions I to III are illustrated in Fig. S8.

The proton storage behavior in β-MnO_2@GO can be further confirmed by XPS analyses. Before the XPS tests, the ZSH on electrode is removed by dilute acid to eliminate the influence of by-products. Figure 3h shows the evolution of O 1s spectra in initial two cycles, where the peaks near 531.9 eV (referring to Mn–O–H bonds on [MnO_6] octahedron units) increase upon discharge and decrease upon charge, which is correlated with the regular variation in Mn valence (Fig. S9). Accompanying with the proton insertion/extraction processes, the inevitable Mn^{3+} disproportionation occurs upon discharge. As a consequence, some Mn^{2+} ions dissolve and migrate into the electrolyte, resulting in Mn vacancies on the surface of β-MnO_2. In the subsequent discharge process, Zn^{2+} ions can easily insert into the defective structure and give rise to the transformation into $Zn_xMn_2O_4$ ($x < 1$) spinel phase in the surface region.

Figure 3i shows the evolution of Zn 2p spectra in the initial two cycles. It can be seen that the Zn 2p peaks become obvious starting from the second discharge process (since point #F), indicating that Zn^{2+} cannot insert into the lattice framework of β-MnO_2 until there are some Mn vacancies generated after the first discharge process. The Zn^{2+} ions in $Zn_xMn_2O_4$ are largely unextractable, demonstrating a low reversibility of Zn^{2+} insertion/extraction. Similar charge storage behavior in β-MnO_2 is also characterized in Figs. S10–S12. Moreover, after long-term cycles, the proton storage reactions still dominate the charge storage of β-MnO_2@GO electrode (Figs. S13–S15, Tables S2, S3) despite such structural evolution. V_O and SC will significantly influence the proton storage behavior and $Zn_xMn_2O_4$ formation process, which will be discussed in the following part.
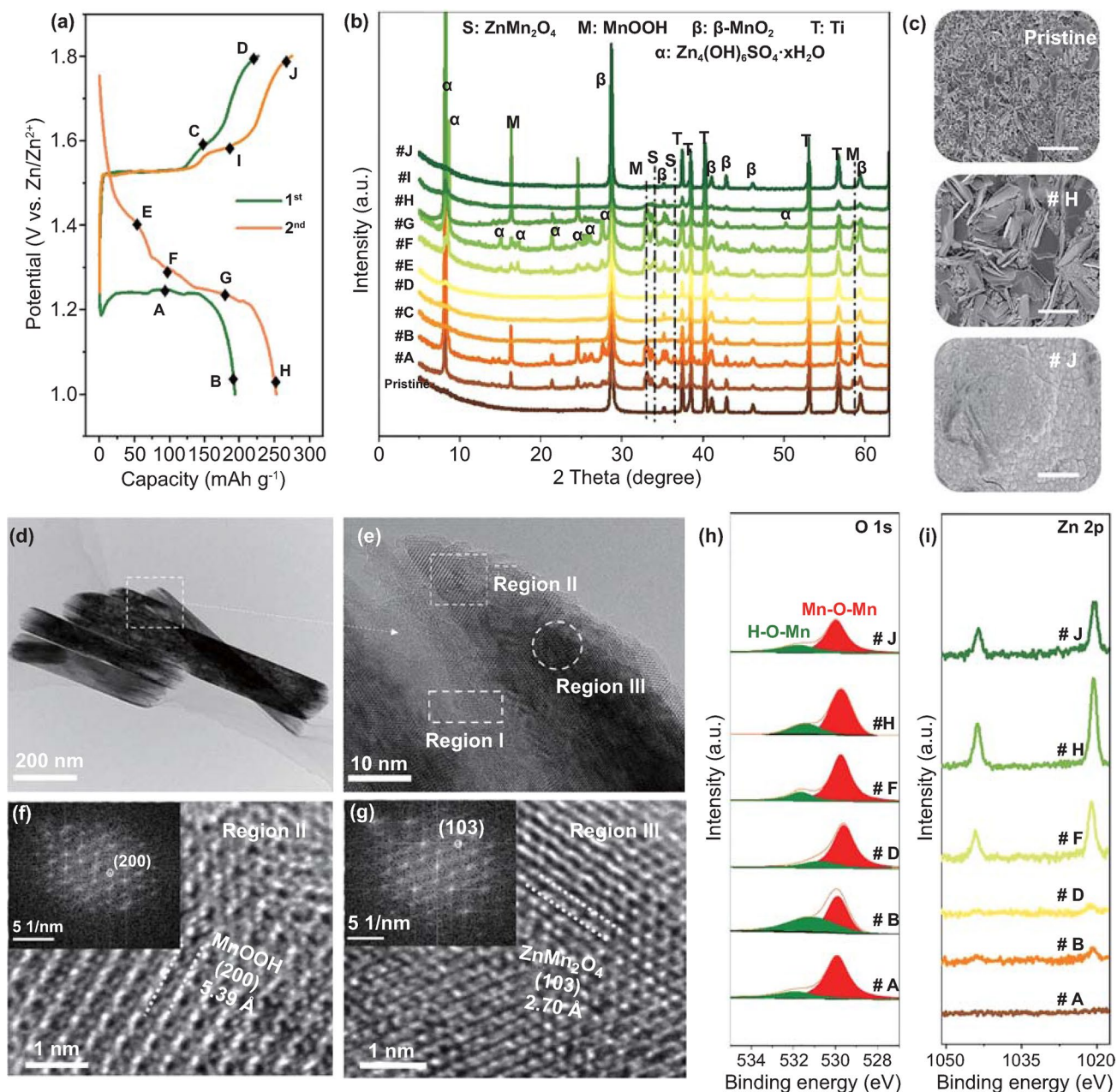
Fig. 3 **a** Galvanostatic charge/discharge curves at 0.1C in the initial two cycles, and **b, c** XRD patterns and SEM morphologies of β-MnO$_2$@GO electrode at pristine, points #H and #J. **d–g** TEM and HRTEM images of β-MnO$_2$@GO at fully discharged state in the first cycle. **h, i** XPS analyses of O 1s and Zn 2p spectra at selected points. Scale bars in **c** are ∼ 2 μm

3.4 Superior Reaction Kinetics

As displayed in Fig. 2a, the boosted rate performance is mainly attributed to the incorporation of V$_O$ in β-MnO$_2$@ GO. Figure 4a shows the calculated electron density of states of β-MnO$_2$ and β-MnO$_2$ + V$_O$ by DFT calculations.

The pristine β-MnO$_2$ has a bandgap of ∼ 0.25 eV, while a lower value of ∼ 0.12 eV is obtained after introducing a V$_O$ in the supercell, indicating an enhanced electronic conductivity of β-MnO$_2$ + V$_O$. Consistent with the above result, the β-MnO$_2$@GO electrode presents much lower charge transfer impedance of ∼ 365.3 Ω cm^2 when compared with that of the
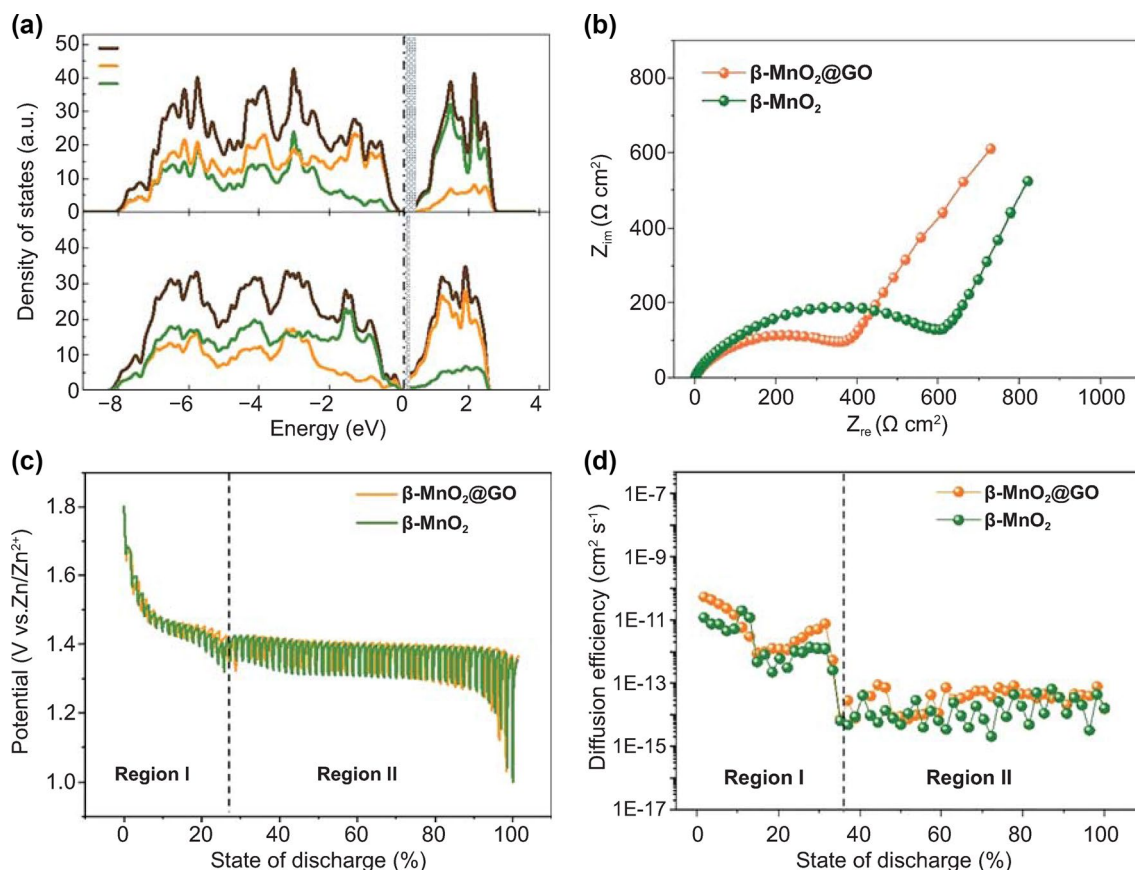
Fig. 4 **a** Calculated electron density of states of β-MnO$_2$ with and without V$_O$. Energies are referenced to the Fermi level. **b** EIS spectra of electrodes with β-MnO$_2$ and β-MnO$_2$@GO as active materials. **c, d** GITT curves and calculated diffusion coefficients

β-MnO$_2$ electrode (~604.3 Ω cm^2). The galvanostatic intermittent titration technique (GITT) measurements are further applied to illustrate the proton insertion kinetics (Fig. 4c, d), and the detailed calculation processes of diffusion coefficients are illustrated in SI. The β-MnO$_2$@GO electrode shows average diffusion coefficients of ~1.13×10^{-11} cm^2 s^{-1} in region I (from 1.8 to 1.35 V) and ~4.00×10^{-14} cm^2 s^{-1} in region II (from 1.35 to 1.05 V), which are consistently higher than that of β-MnO$_2$ electrode (~4.25×10^{-12} cm^2 s^{-1} in region I and ~2.57×10^{-14} cm^2 s^{-1} in region II).

3.5 Enhanced Cycling Stability

As illustrated in Fig. 2d, e, the GO wrapping can dramatically enhance the cycling stability. In this part, the mechanism of such enhancement is comprehensively investigated. DFT calculations are applied to reveal the interaction between β-MnO$_2$ and GO. In the absence of an ether oxygen

on GO, the graphene layer is weakly bound to the β-MnO$_2$ surfaces via van der Waals forces, with adsorption energies ranging from 0.21 to 0.44 eV (Fig. S16). Surface V$_O$ of β-MnO$_2$ cannot contribute to sufficiently strong interaction. However, when there exist surface V$_O$ and an ether oxygen in the vicinity, chemical bonding is established featuring Mn–O–C configuration, which pushes the adsorption energy to as high as 0.95–1.52 eV (Fig. 5a). It can be drawn that V$_O$ in β-MnO$_2$ and ether oxygen on GO work in synergy to achieve an intimate self-assembled wrapping of GO on β-MnO$_2$, which provides a direct physical barrier rendering the Mn ions tightly confined beneath the surfaces even at low valence states.

Figure 5b shows the structure evolution of the β-MnO$_2$ electrodes. During cycling, the characteristic peaks of β-MnO$_2$ at 28.7° and 37.5° decrease gradually and disappear after 50 cycles. Meanwhile, the characteristic peaks of ZnMn$_2$O$_4$ at 18.7° and 36.3° emerge and increase gradually
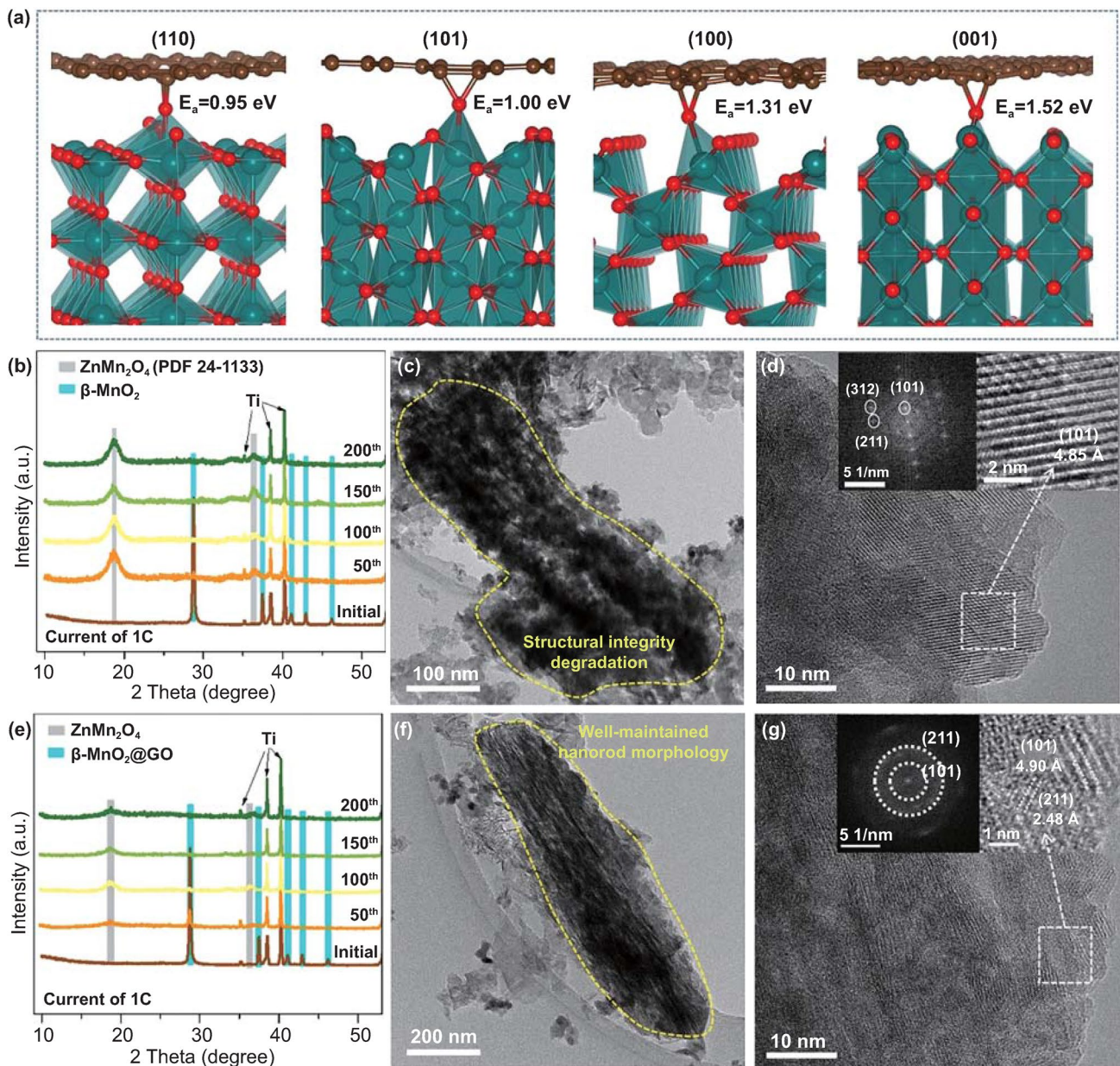
Fig. 5 **a** DFT calculated binding configuration and adsorption energies (E_a) of GO on β-MnO_2 (110), (101), (100), and (001) terraces with a surface V_O. **b** XRD patterns of β-MnO_2 electrodes of pristine and at charged state after 50, 100, 150, and 200 cycles at current of 1C. **c, d** TEM morphologies of active material in β-MnO_2 electrode after 200 cycles at current of 1C, showing a degradation on structural integrity, and the corresponding HRTEM images (inset, diffraction pattern of $ZnMn_2O_4$ spinel). **e** XRD patterns of β-MnO_2@GO electrodes of pristine and at charged state after 50, 100, 150, and 200 cycles at current of 1C. **f, g** TEM morphologies of active material in β-MnO_2@GO electrode after 200 cycles at current of 1C, showing a well-maintained nanorod morphology, and the corresponding HRTEM images (inset, diffraction rings showing (211) and (101) planes of nanocrystalline $Zn_xMn_2O_4$ spinel)

upon cycling. These results indicate a progressive structure evolution from bulk β-MnO_2 to $ZnMn_2O_4$ spinel. Figure 5c, d shows the TEM/HRTEM images and correlated diffraction pattern of the active material in β-MnO_2 after 200 cycles. We observe a severe degradation on the structural

integrity of β-MnO_2, and the active material has completely converted into a bulk (or long-range-ordered) $Zn_xMn_2O_4$ spinel ($x = 1.000$, from ICP result), as confirmed by the clear lattice fringe of (101) plane, as well as the apparent diffraction spots representing the (101), (211), and (312)

plane (diffraction pattern shown in the inset of Fig. 5d). The TEM EDS mapping in Fig. S17 further indicates the uniform distribution of Zn, O, and Mn elements, substantiating the generation of $ZnMn_2O_4$ spinel after long-term cycling.

For β-MnO_2@GO, the structural evolution is different from that of the β-MnO_2, as illustrated in Fig. 5e. The characteristic peaks of β-MnO_2@GO retain well after 100 cycles, demonstrating the beneficial effect of GO wrapping on stabilizing the pristine lattice framework. The relative intensities of the characteristic peaks of $ZnMn_2O_4$ in β-MnO_2@GO electrode are much lower than that in β-MnO_2 electrode, indicating that GO wrapping can effectively inhibit $ZnMn_2O_4$ accumulation upon long-term cycling. The nanorod morphology of β-MnO_2@GO is well preserved even after 200 cycles (Fig. 5f), showing an enhanced structural integrity. Figure 5g shows the HRTEM morphologies and correlated diffraction patterns of the active material, which shows vague lattice fringes referring to the (101) and (211) planes of $Zn_xMn_2O_4$ ($x=0.846$, from ICP result) spinel with lattice spacing of ~ 4.90 Å and ~ 2.48 Å, respectively. The correlated diffraction pattern shows two diffraction rings (inset in Fig. 5g), indicating the nanocrystalline (or short-term ordered) feature that favors proton intercalation/conversion reactions. EDS mapping results show a uniformly distributed Zn, O, and Mn elements in the active material of β-MnO_2@GO electrode after 200 cycles (Fig. S18), confirming the generation of nanocrystalline $ZnMn_2O_4$.

Overall, the combinatorial incorporation of V_O and SC in β-MnO_2 could help in achieving better electrochemical performance on the following mechanistic aspects: (1) both V_O and GO wrapping could facilitate electron transport; (2) intimate adhesion of GO on the defective surface could pose barrier to the dissolution of Mn ions; (3) combination of V_O and GO wrapping can retard the $Zn_xMn_2O_4$ accumulation and regulate the structural evolution.

4 Conclusions

In this work, the concurrent application of both defect engineering and interfacial optimization to a manganese oxide electrode for AZIBs is for the first time demonstrated. Oxygen vacancies are spontaneously introduced into β-MnO_2 during its synthesis in the presence of GO that eventually builds a coating layer on the active material. For the as-prepared oxygen-deficient β-MnO_2@GO cathode, the successful suppression of Mn dissolution during electrochemical cycling is made possible, along with an apparent enhancement in charge/discharge kinetics. This electrode delivers a capacity of ~ 129.6 mAh g^{-1} even after 2000 cycles at a current rate of 4C, which is much superior than that of pristine β-MnO_2 electrode. The excellent cycle stability is rooted in the strong binding between the surface V_O and ether oxygen on GO, as well as the regulated structural evolution into the nanocrystalline $Zn_xMn_2O_4$ phase. The results in this work highlight the advantages of integrating multiple strategies in the design of AZIB electrodes via bottom-up synthetic approaches, which will cast light on the feasibility of AZIBs in meeting the high-rate and long-life requirements for large-scale energy storage applications.

References

1. G. Fang, J. Zhou, S. Liang et al., Recent advances in aqueous zinc-ion batteries. ACS Energy Lett. **3**(10), 2480–2501 (2018). https://doi.org/10.1021/acsenergylett.8b01426

2. L. Blanc, D. Kundu, L. Nazar, Scientific challenges for the implementation of Zn-ion batteries. Joule **4**, 1–29 (2020). https://doi.org/10.1016/j.joule.2020.03.002

3. C. Xu, B. Li, H. Du, F. Kang, Energetic zinc ion chemistry: the rechargeable zinc ion battery. Angew. Chem. Int. Ed. **51**(4), 933–935 (2012). https://doi.org/10.1002/anie.201106307

4. D. Kundu, B. Dams, V. Duffort, S. Vajargah, L. Nazar, A high-capacity and long-life aqueous rechargeable zinc battery using a metal oxide intercalation cathode. Nat. Energy **1**(10), 16119 (2016). https://doi.org/10.1038/NENERGY.2016.119

5. Q. Yang, F. Mo, Z. Liu, S. Chen, S. Zhang et al., Activating C-coordinated iron of iron hexacyanoferrate for Zn hybrid-ion batteries with 10000-cycle lifespan and superior rate capability. Adv. Mater. **31**(32), 1901521 (2019). https://doi.org/10.1002/adma.201901521

6. X. Wu, Y. Xu, C. Zhang, D. Leonard, A. Markir et al., Reverse dual-ion battery via a $ZnCl_2$ water-in-salt electrolyte. J. Am. Chem. Soc. **141**, 6338–6344 (2019). https://doi.org/10.1021/jacs.9b00617

7. S. Huang, F. Wan, S. Bi, J. Zhu, Z. Niu et al., A self-healing integrated all-in-one zinc-ion battery. Angew. Chem. Int. Ed. **58**(13), 4313–4317 (2019). https://doi.org/10.1002/ange.201814653

8. B. Lee, C. Yoon, H. Lee, K. Chung, B. Cho et al., Electrochemically-induced reversible transition from the tunneled to layered polymorphs of manganese dioxide. Sci. Rep. **4**, 6066 (2014). https://doi.org/10.1038/srep06066

9. N. Zhang, F. Cheng, J. Liu, L. Wang, X. Long et al., Rechargeable aqueous zinc-manganese dioxide batteries with high energy and power densities. Nat. Commun. **8**(1), 405 (2016). https://doi.org/10.1038/s41467-017-00467-x

10. C. Wang, Y. Zeng, X. Xiao, S. Wu, G. Zhong et al., γ-MnO_2 nanorods/graphene composite as efficient cathode for advanced rechargeable aqueous zinc-ion battery. J. Energy Chem. **43**, 182–187 (2020). https://doi.org/10.1016/j.jechem.2019.08.011

11. J. Huang, Z. Wang, M. Hou, X. Dong, Y. Liu et al., Polyaniline-intercalated manganese dioxide nanolayers as a high-performance cathode material for an aqueous zinc-ion battery. Nat. Commun. **9**(1), 2906 (2018). https://doi.org/10.1038/s41467-018-04949-4

12. N. Zhang, F. Cheng, Y. Liu, Q. Zhao, K. Lei et al., Cation-deficient spinel $ZnMn_2O_4$ cathode in $Zn(CF_3SO_3)_2$ electrolyte for rechargeable aqueous Zn-ion battery. J. Am. Chem. Soc. **138**(39), 12894–12901 (2016). https://doi.org/10.1021/jacs.6b05958

13. Y. Xu, X. Deng, Q. Li, G. Zhang, F. Xiong et al., Vanadium oxide pillared by interlayer Mg^{2+} ions and water as ultralong-life cathodes for magnesium-ion batteries. Chem **5**, 1194–1209 (2019). https://doi.org/10.1016/j.chempr.2019.02.014

14. N. Zhang, X. Chen, M. Yu, Z. Niu, F. Cheng et al., Materials chemistry for rechargeable zinc-ion batteries. Chem. Soc. Rev. **49**, 4203–4219 (2020). https://doi.org/10.1039/c9cs00349e

15. Q. Zhao, A. Song, S. Ding, R. Qin, Y. Cui et al., Pre-intercalation strategy in manganese oxides for electrochemical energy storage: review and prospect. Adv. Mater. **32**, 2002450 (2020). https://doi.org/10.1002/adma.202002450

16. T. Xiong, Y. Zhang, W. Lee, J. Xue et al., Defect engineering in manganese-based oxides for aqueous rechargeable zinc-ion batteries: a review. Adv. Energy Mater. **10**, 2001769 (2020). https://doi.org/10.1002/aenm.202001769

17. Y. Tian, X. Liu, L. Xu, D. Yuan, Y. Dou et al., Engineering crystallinity and oxygen vacancies of Co(II) oxide nanosheets for high performance and robust rechargeable Zn–air batteries. Adv. Funct. Mater. **31**, 2101239 (2021). https://doi.org/10.1002/adfm.202101239

18. X. Zhang, J. Li, Y. Qian et al., Appropriately hydrophilic/hydrophobic cathode enables high-performance aqueous zinc-ion batteries. Energy Storage Mater. **30**, 337–345 (2020). https://doi.org/10.1016/j.ensm.2020.05.021

19. Y. Tian, L. Xu, M. Li, D. Yuan, X. Liu et al., Interface engineering of CoS/CoO@N-doped graphene nanocomposite for high-performance rechargeable Zn–Air batteries. Nano-Micro Lett. **13**, 3 (2021). https://doi.org/10.1007/s40820-020-00526-x

20. Q. Zhao, A. Song, W. Zhao, R. Qin, S. Ding et al., Boosting the energy density of aqueous batteries via facile grotthuss proton transport. Angew. Chem. Int. Ed. **132**, 2–8 (2020). https://doi.org/10.1002/ange.202011588

21. N. Liu, X. Wu, Y. Yin, Y. Chen, A. Zhao et al., Constructing the efficient ion diffusion pathway by introducing oxygen defects in Mn_2O_3 for high-performance aqueous zinc-ion batteries. ACS Appl. Mater. Interfaces **12**(25), 28199–28205 (2020). https://doi.org/10.1021/acsami.0c05968

22. Q. Tan, X. Li, B. Zhang, X. Chen, Y. Tian et al., valence engineering via in situ carbon reduction on octahedron sites Mn_3O_4 for ultra-long cycle life aqueous Zn-ion battery. Adv. Energy Mater. **10**(38), 2001050 (2019). https://doi.org/10.1002/aenm.202001050

23. T. Xiong, Z. Yu, H. Wu, Y. Du, Q.J. Chen et al., Defect engineering of oxygen-deficient manganese oxide to achieve high-performing aqueous zinc ion battery. Adv. Energy Mater. **9**(14), 1803815 (2019). https://doi.org/10.1002/aenm.201803815

24. J. Wang, X. Qin, Y. Wang, M. Shao et al., Superfine MnO_2 nanowires with rich defects toward a boosted zinc ion storage performance. ACS Appl. Mater. Interfaces **12**, 34949–34958 (2020). https://doi.org/10.1021/acsami.0c08812

25. G. Fang, C. Zhu, M. Chen, J. Zhou, B. Tang et al., Suppressing manganese dissolution in potassium manganate with rich oxygen defects engaged high-energy-density and durable aqueous zinc-ion battery. Adv. Funct. Mater. **29**(15), 1808375 (2019). https://doi.org/10.1002/adfm.201808375

26. H. Zhang, J. Wang, Q. Liu, W. He, Z. Lai et al., Extracting oxygen anions from $ZnMn_2O_4$: robust cathode for flexible all-solid-state Zn-ion batteries. Energy Storage Mater. **21**, 154–161 (2019). https://doi.org/10.1016/j.ensm.2018.12.019

27. M. Han, J. Huang, S. Liang, L. Shan, X. Xie et al., Oxygen defects in beta-MnO_2 enabling high-performance rechargeable aqueous zinc/manganese dioxide battery. iScience **23**(1), 100797 (2020). https://doi.org/10.1016/j.isci.2019.100797

28. B. Wu, G. Zhang, M. Yan, T. Xiong, L. Mai, Graphene scroll-coated alpha-MnO_2 nanowires as high-performance cathode materials for aqueous Zn-ion battery. Small **14**(13), 1703850 (2018). https://doi.org/10.1016/10.1002/smll.201703850

29. W. Jiang, X. Xu, Y. Liu, F. Zhou, Z. Xu et al., Facile plasma treated β-MnO_2@C hybrids for durable cycling cathodes in aqueous Zn-ion batteries. J. Alloy. Compd. **827**, 154273 (2020). https://doi.org/10.1016/j.jallcom.2020.154273

30. Q. Zhao, X. Huang, M. Zhou, Z. Ju, X. Sun et al., Proton insertion promoted polyfurfural/MnO_2 nanocomposite cathode for

rechargeable aqueous Zn-MnO$_2$ battery. ACS Appl. Mater. Interfaces **12**(32), 36072–36081 (2020). https://doi.org/10.1021/acsami.0c08579

31. J. Huang, X. Tang, K. Liu, G. Fang, Z. He et al., Interfacial chemical binding and improved kinetics assisting stable aqueous Zn–MnO$_2$ batteries. Mater. Today Energy **17**, 100475 (2020). https://doi.org/10.1016/j.mtener.2020.100475

32. W. Chen, X. Feng, J. Chen, L. Yan, Power-output reduction of graphene oxide and a MnO$_2$-free Zn/GO primary cell. RSC Adv. **4**(80), 42418–42423 (2014). https://doi.org/10.1016/10.1039/c4ra06354f

33. Y. Zhang, S. Deng, G. Pan, H. Zhang, B. Liu et al., Introducing oxygen defects into phosphate ions intercalated manganese dioxide. Small Methods **4**(6), 1900828 (2020). https://doi.org/10.1002/smtd.201900828

34. M. Long, Y. Qin, C. Chen, X. Guo, B. Tan et al., Origin of visible light photoactivity of reduced graphene oxide/TiO$_2$ by in situ hydrothermal growth of undergrown TiO$_2$ with graphene oxide. J. Phys. Chem. C **117**(23), 16734–16741 (2013). https://doi.org/10.1021/jp4058109

35. M. Sun, X. Dong, B. Lei, J. Li, P. Chen et al., Graphene oxide mediated Co-generation of C-doping and oxygen defects in Bi$_2$WO$_6$ nanosheets: a combined DRIFTS and DFT investigation. Nanoscale **11**, 20562 (2019). https://doi.org/10.1039/C9NR06874K

36. M. Zhu, Y. Cai, S. Liu, M. Fang, X. Tan et al., K$_2$Ti$_6$O$_{13}$ hybridized graphene oxide: effective enhancement in photodegradation of RhB and photoreduction of U(VI). Environ.

Pollut. **248**, 448–455 (2019). https://doi.org/10.1016/j.envpol.2019.02.025

37. X. Lei, X. Li, Z. Ruan, T. Zhang, F. Pan et al., Adsorption-photocatalytic degradation of dye pollutant in water by graphite oxide grafted titanate nanotubes. J. Mol. Liq. **266**, 122–131 (2018). https://doi.org/10.1016/j.molliq.2018.06.053

38. M. Liu, Q. Zhao, H. Liu, J. Yang, X. Chen et al., Tuning phase evolution of β-MnO$_2$ during microwave hydrothermal synthesis for high-performance aqueous Zn ion battery. Nano Energy **64**, 103942 (2019). https://doi.org/10.1016/j.nanoen.2019.103942

39. Q. Zhao, X. Chen, Z. Wang, L. Yang, R. Qin et al., Unravelling H$^+$/Zn^{2+} synergistic intercalation in a novel phase of manganese oxide for high-performance aqueous rechargeable battery. Small **15**, 1904545 (2019). https://doi.org/10.1002/smll.201904545

40. N. Li, G. Li, C. Li, H. Yang, G. Qin et al., Bi-cation electrolyte for a 1.7 V aqueous Zn ion battery. ACS Appl. Mater. Interfaces **12**(12), 13790–13796 (2020). https://doi.org/10.1021/acsami.9b20531

41. H. Pan, Y. Shao, Y. Chen, K. Han, Z. Nie et al., Reversible aqueous zinc/manganese oxide energy storage from conversion reactions. Nat. Energy **1**(5), 16039 (2016). https://doi.org/10.1038/NENERGY.2016.39

42. M. Chamoun, W. Brant, C. Tai, D. Noréus et al., Rechargeability of aqueous sulfate Zn/MnO$_2$ batteries enhanced by accessible Mn^{2+} ions. Energy Storage Mater. **15**, 351–360 (2018). https://doi.org/10.1016/j.ensm.2018.06.019